Vietnam Journal of Mechanics, Vol. 47, No. 2 (2025), pp. 142 – 153
DOI: https://doi.org/10.15625/0866-7136/22179

FORMING LIMIT PREDICTION OF ADVANCED HIGH-STRENGTH STEELS (AHSS) USING AN ENHANCED DUCTILE DAMAGE MODEL

Hao H. Nguyen
Campus in Ho Chi Minh City, University of Transport and Communications, No. 450-451 Le Van Viet street, Thu Duc city, Ho Chi Minh city, Vietnam
E-mail: haonh@utc.edu.vn

Received: 06 January 2025 / Revised: 26 February 2025 / Accepted: 06 March 2025
Published online: 29 March 2025

Abstract. This paper presents prediction of forming limits of Advanced High-Strength Steels (AHSS) DP980 by adopting an enhanced ductile damage model to consider sheet metal anisotropy. The micro-void growth-based original damage model is transformed from principal stress space (σ_1, σ_2, σ_3) into the equivalent stress, Lode parameter, and stress triaxiality space (σ_e, L_p, η). The proposed ductile fracture prediction model is then implemented and integrated with a finite element (FE) software package to conduct the deep drawing numerical simulations. The Nakajima-type specimens are adopted to predict the limiting principal plastic strains ranging from uniaxial tensile through plane-strain to biaxial tensile loading states. The forming limit diagram (FLD) of DP980 steel is established in accordance with the ISO 12004-2-2008 standard.

Keywords: ductile fracture, forming limit diagram, AHSS steel, ductile damage model.

1. INTRODUCTION

The fracture mechanism of metallic materials has been proven to be due to micro-void initiation, growth, and coalescence [1]. A void growth-based ductile fracture criterion, which is most widely applied for predicting crack initiation in various materials was developed by Gurson [2]. The ductile fracture is known as the simultaneous domination of the Lode parameter and the stress triaxiality on the plastic strain path [3,4]. Pathak et al. [5] investigated the influence of triaxiality and the Lode parameter on the nucleation behavior of the DP780 and CP800 steel sheets. Accordingly, for both material types, at a specific strain level, the number of voids per unit volume is highest during the biaxial

dome test while void nucleation is lowest during the simple shear test. The AHSS sheets have been widely used in the automotive, maritime, and civil industries due to their excellent strength, good crash energy absorption, and high corrosion resistance. Nevertheless, they are formed by hot and cold rolling processes leading to changes in the crystal structure which is the root of anisotropic properties, meaning plasticity in various orientations is not the same. Li et al. [6] investigated the anisotropic fracture behavior of AHSS sheet in a large range of stress states from the stress states from simple shear, and uniaxial tension, to plane strain tension and concluded that the anisotropic fracture behavior of AHSS steel is highly dependent on the stress states. The plastic damage criteria can be established based on stress or strain states [7]. By observing deformed microstructures under different strain conditions in several types of High Strength Low Alloy (HSLA), Dual Phase (DP), and Transformation Induced Plasticity (TRIP) steel, Nikhare et al. [8] showed that there are very different forming and fracture behaviors depending on the deformation mode.

With the rapid proliferation of 3rd generation AHSS steels to satisfy modern manufacturing demands, in some cases, the previous ductile fracture prediction models are no longer suitable for accurately predicting the crack initiation of these advanced materials. This has motivated a community of researchers to improve existing ductile damage criteria and continue to propose novel crack prediction models. Zhang et al. [9] modified the DF2010 ductile fracture criterion to formulate a semi-coupled ductile fracture model for DP590 steel. The new model shows the accurate predictability of the fracture behavior of DP590 materials under different stress states. Aydiner et al. [10] adopted the crystal plasticity and cohesive zone frameworks conjugated with a ductile failure model in 3D polycrystalline materials to investigate the failure mechanism of dual-phase (DP) steels via representative volume element (RVE) simulations.

The ductile fracture models mentioned above do not simultaneously include the influences of the Lode parameter, stress triaxiality, and equivalent stress space during the loading process. The current study introduces an enhanced ductile fracture model that considers the simultaneous effects of the Lode parameter and stress triaxiality on forming behavior. Specifically, the anisotropic high-strength sheet steel DP980 is adopted to validate the proposed model's applicability for predicting the deformation-based forming limit curve.

2. DUCTILE FRACTURE MODEL

2.1. Micro-void growth-based ductile damage criterion

A crack criterion based on micro-void growth in elastoplastic materials obeying a power hardening rule has been proposed by Dung [11]. Three void growth rates in principal stress space are presented as follows

$$\mathrm{d}D_1 = \left\{ \left[\frac{\sqrt{3}}{(1-m)} \sinh\left(\frac{\sqrt{3}\,(1-m)}{4} \frac{\sigma_1+\sigma_2+\sigma_3}{\sigma_f} \right) \times \cosh\left(\frac{\sqrt{3}\,(1-m)}{4} \frac{\sigma_2-\sigma_3}{\sigma_f} \right) \right] + \frac{3}{4} \frac{\sigma_1-\sigma_2-\sigma_3}{\sigma_f} \right\} \mathrm{d}\bar{\varepsilon}^p, \tag{1}$$

$$\mathrm{d}D_2 = \left\{ \left[\frac{\sqrt{3}}{(1-m)} \sinh\left(\frac{\sqrt{3}\,(1-m)}{4} \frac{\sigma_1+\sigma_2+\sigma_3}{\sigma_f} \right) \times \cosh\left(\frac{\sqrt{3}\,(1-m)}{4} \frac{\sigma_1-\sigma_3}{\sigma_f} \right) \right] + \frac{3}{4} \frac{\sigma_2-\sigma_1-\sigma_3}{\sigma_f} \right\} \mathrm{d}\bar{\varepsilon}^p, \tag{2}$$

$$\mathrm{d}D_3 = \left\{ \left[\frac{\sqrt{3}}{(1-m)} \sinh\left(\frac{\sqrt{3}\,(1-m)}{4} \frac{\sigma_1+\sigma_2+\sigma_3}{\sigma_f} \right) \times \cosh\left(\frac{\sqrt{3}\,(1-m)}{4} \frac{\sigma_1-\sigma_2}{\sigma_f} \right) \right] + \frac{3}{4} \frac{\sigma_3-\sigma_1-\sigma_2}{\sigma_f} \right\} \mathrm{d}\bar{\varepsilon}^p, \tag{3}$$

where σ_i $(i = 1, 2, 3)$ denote principal stress components, $d\bar{\varepsilon}^p$ is the equivalent plastic strain increment, and m is a material parameter relative to the hardening property of matrix material.

Assuming that the ductile fracture initiates once the damage accumulated variable reaches a critical value

$$D_g = \max\left(D_1, D_2, D_3\right) = \max\left(\int_0^{\bar{\varepsilon}_f^p} \left(\mathrm{d}D_1, \mathrm{d}D_2, \mathrm{d}D_3\right) \right) = D_g^f, \tag{4}$$

where $\bar{\varepsilon}_f^p$ is the equivalent plastic strain at fracture, D_g^f is a damage constant depending on specific material.

2.2. Enhanced ductile damage model

Assuming that the material anisotropy obeys the second-order yield criterion Hill48, the equivalent stress of matrix material is presented in the Cauchy stress space as below

$$\sigma_e = \left[H\left(\sigma_{11}-\sigma_{22}\right)^2 + F\left(\sigma_{22}-\sigma_{33}\right)^2 + G\left(\sigma_{33}-\sigma_{11}\right)^2 + 2N\sigma_{12}^2 + 2L\sigma_{23}^2 + 2M\sigma_{31}^2 \right]^{1/2}, \tag{5}$$

where σ_{ij} $(i, j = 1, 2, 3)$ denote normal and shear components of the Cauchy stress tensor; H, F, G, N, L, and M are the anisotropic parameters determined from Lankford's

coefficients r_0, r_{45}, r_{90} as follows

$$\begin{aligned} F &= \frac{r_0}{r_{90}\left(r_0+1\right)}, \quad G = \frac{1}{r_0+1}, \quad H = \frac{r_0}{r_0+1}, \\ L &= M = \frac{3}{2}, \quad N = \frac{\left(r_0+r_{90}\right)\left(1+2r_{45}\right)}{2r_{90}\left(1+r_0\right)}. \end{aligned} \tag{6}$$

The coefficients r_0, r_{45}, and r_{90} are identified from uniaxial tensile test.

The principal stresses can be written by the functions of the Lode parameter and stress triaxiality as below

$$\begin{aligned} \sigma_1 &= \sigma_m + s_1 = \left(\eta + \frac{3-L_p}{6\sqrt{T}}\right)\sigma_e, \\ \sigma_2 &= \sigma_m + s_2 = \left(\eta + \frac{2L_p}{6\sqrt{T}}\right)\sigma_e, \\ \sigma_3 &= \sigma_m + s_3 = \left(\eta - \frac{3+L_p}{6\sqrt{T}}\right)\sigma_e, \end{aligned} \tag{7}$$

where $\sigma_m = \left(\sigma_1+\sigma_2+\sigma_3\right)/3$ is mean stress; $s_i = \sigma_i - \sigma_m, (i = 1,2,3)$ are principal deviatoric stresses, T is an equivalent stress function introduced by Park et al. [7] and given in Eq. (8), L_P is the Lode parameter, η is stress triaxiality, θ is the angle between the rolling direction and the maximum principal stress direction. Fig. 1 illustrates the discrepancy between the rolling direction (RD), the transverse direction (TD), and the normal direction (ND) compared with the principal directions $(\sigma_1, \sigma_2, \sigma_3)$.

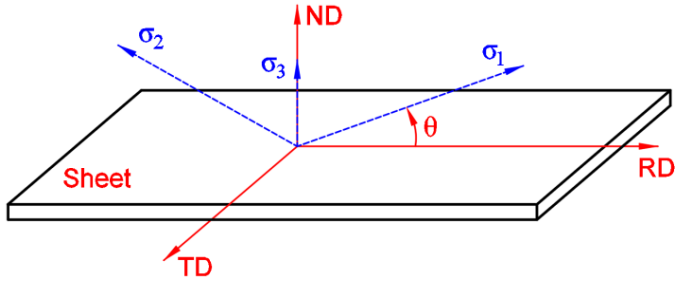

Fig. 1. Presentation of principal directions to sheet material

$$\begin{aligned} T = {} & F\left(\frac{1+L_p}{2}\cos^2\theta + \sin^2\theta\right)^2 + G\left(\cos^2\theta + \frac{1+L_p}{2}\sin^2\theta\right)^2 \\ & + \left(H\cos^2 2\theta + \frac{N}{2}\sin^2 2\theta\right)\left(\frac{1-L_p}{2}\right)^2. \end{aligned} \tag{8}$$

Assuming that $\sigma_1 \geq \sigma_2 \geq \sigma_3$, the Hill48 equivalent stress and Lode parameter can be calculated as follows

$$\sigma_e = \sqrt{T\left(\sigma_1 - \sigma_3\right)^2} \quad \text{and} \quad L_p = \frac{2\sigma_2 - \sigma_1 - \sigma_3}{\sigma_1 - \sigma_3}. \tag{9}$$

Substituting Eq. (7) into Eqs. (1), (2), and (3), three void growth rates as functions depending on the Lode parameter, stress triaxiality, and equivalent stress (L_p, η, σ_e) only are archived as follows

$$\begin{aligned} dD_a = &\left[\frac{\sqrt{3}}{(1-m)}\sinh\left(\frac{3\sqrt{3}\,(1-m)\,\eta R_s}{4}\right)\right. \\ &\left.\times\cosh\left(\frac{\sqrt{3}\,(1-m)\,(1+L_p)\,R_s}{8\sqrt{T}}\right) + \frac{3R_s}{4}\left(\frac{3-L_p}{3\sqrt{T}} - \eta\right)\right]\mathrm{d}\bar{\varepsilon}_e^p, \end{aligned} \tag{10}$$

$$\begin{aligned} dD_b = &\left[\frac{\sqrt{3}}{(1-m)}\sinh\left(\frac{\sqrt{3}\,(1-m)\,\eta R_s}{4}\right)\right. \\ &\left.\times\cosh\left(\frac{\sqrt{3}\,(1-m)\,R_s}{4\sqrt{T}}\right) + \frac{3R_s}{4}\left(\frac{2L_p}{3\sqrt{T}} - \eta\right)\right]\mathrm{d}\bar{\varepsilon}_e^p, \end{aligned} \tag{11}$$

$$\begin{aligned} dD_c = &\left[\frac{\sqrt{3}}{(1-m)}\sinh\left(\frac{\sqrt{3}\,(1-m)\,\eta R_s}{4}\right)\right. \\ &\left.\times\cosh\left(\frac{\sqrt{3}\,(1-m)\,R_s}{4}\left(\frac{1-L_p}{2\sqrt{T}}\right)\right) + \frac{3R_s}{4}\left(\frac{3+L_p}{3\sqrt{T}} + \eta\right)\right]\mathrm{d}\bar{\varepsilon}_e^p, \end{aligned} \tag{12}$$

where $R_s = \sigma_e/\sigma_f$ denotes the ratio between the equivalent stress and the yield stress of the material, $\eta = \sigma_m/\sigma_e$ is stress triaxiality.

The original damage model did not consider ductile fracture under a very low-stress triaxiality state, that is the value η of zero. McClintock [12] introduced a damage variable due to shearing and rotating voids during material deformation as follows

$$\varepsilon_s = \ln\left(\frac{\ell}{2r}\right) = \ln\left(\frac{\ell_0}{2r_0}\right) - \frac{1}{D_g^f}\int \mathrm{d}D_i\,, \quad i = 1,2,3 \tag{13}$$

where ℓ_0 is the space between two adjacent voids, r_0 is the initial void radius when the material has not yet been deformed.

To consider void-by-void interaction, Xue [13] proposed an artificial strain

$$\varepsilon_{art} = \ln\sqrt{1+\gamma^2} = \ln\sqrt{1+2N\left(\bar{\varepsilon}^p\right)^2}. \tag{14}$$

This work introduced a shear damage variable as below

$$D_s = \frac{\varepsilon_{art}}{\varepsilon_s} = \frac{\ln\sqrt{1+2N\left(\bar{\varepsilon}^p\right)^2}}{\ln\left(\dfrac{\ell_0}{2r_0}\right) - \dfrac{1}{D_g^f}\displaystyle\int \mathrm{d}D_i}. \tag{15}$$

The shear damage rate is obtained as follows

$$\mathrm{d}D_s = \frac{2N\bar{\varepsilon}^p}{\left[1+2N\left(\bar{\varepsilon}^p\right)^2\right] \times \left[\ln\left(\dfrac{\ell_0}{2r_0}\right) - D_g\right]}\mathrm{d}\bar{\varepsilon}^p. \tag{16}$$

The damage variable used for the general loading state

$$D_t = \frac{1}{D_{crit}}\left[D_g + g\left(\theta\right)D_s\right]. \tag{17}$$

The enhanced plastic failure model expressed as a function of the stress state together with the damage variable is now ready for predicting fracture.

$$\Phi = \sigma_e - g\left(D\right)\sigma_f = 0, \tag{18}$$

where $g\left(D\right) = 1 - D_t^{\beta}$ is a function representing material mechanical deterioration during the loading process, β is a softening exponent.

3. FORMING LIMIT PREDICTION

3.1. Numerical implementation of ductile fracture model

The proposed damage model is implemented by a user subroutine using a numerical algorithm, namely the "cutting plane" introduced by Ortiz and Simo [14]. The implementation steps are as follows:

Step 1: Calculate the trial stress state using the assumption of an elastic material

$$\sigma_{ij} = C_{ijkl}\Delta\varepsilon_{kl}. \tag{19}$$

Step 2: Calculate the equivalent stress from Cauchy components σ_{ij} and calculate yield stress σ_f using the hardening rule of the material.

Step 3: Check the current stress state. If $\Phi < 0$, the material stress state is elastic; conversely, if $\Phi \geq 0$, the matrix material is considered to have plastically yielded, and the plastic nonlinear problem is solved by the iterative method. The plastic variables need to be calculated as follows:

Plastic multiplier

$$\mathrm{d}\lambda = \frac{\Phi}{\dfrac{\partial \Phi}{\partial \sigma_{ij}} : C_{ijkl} : \dfrac{\partial \Phi}{\partial \sigma_{kl}}}. \tag{20}$$

Plastic strain rate tensor components

$$\mathrm{d}\varepsilon_{ij} = \mathrm{d}\lambda \frac{\partial \Phi}{\partial \sigma_{ij}}. \tag{21}$$

Equivalent plastic strain increment

$$\mathrm{d}\bar{\varepsilon}_e^p = \sqrt{\frac{2}{3}\mathrm{d}\varepsilon_{ij} : \mathrm{d}\varepsilon_{ij}}. \tag{22}$$

The damage evolution rates are calculated by the equations of (10), (11), (12), and (16).

Step 4: Check the convergence.

If $\Phi > 10^{-7}$ convergence condition is not satisfied, so the program goes back to Step 3.

If $\Phi \leq 10^{-7}$ the program will update plastic variables as follows: the equivalent plastic strain $\bar{\varepsilon}_e^p = \bar{\varepsilon}_e^p + \mathrm{d}\bar{\varepsilon}_e^p$, damage variables $D_g = D_g + \mathrm{d}D_g$, $D_s = D_s + \mathrm{d}D_s$ and $D_t = D_g + g(\theta) D_s$, and new stress state $\sigma_{ij} = \sigma_{ij} + \Delta\sigma_{ij}$. This process will be iterated until the occurrence of fracture.

3.2. Numerical simulations

Sheet steel DP980 with a nominal thickness of 0.82 mm is used for validating the applicability of the proposed model. The mechanical properties of DP980 are given in Table 1.

Table 1. Mechanical characteristics of DP980 steel [15]

Young's modulus, E (GPa)	Poisson's ratio, ν	Lankford's coefficients		
		r_0	r_{45}	r_{90}
210	0.3	0.92	0.83	1.04

A hybrid hardening rule which is the combination of a power law Swift and an exponential function Voce has been used in this work as follows

$$\sigma_f = \alpha A \left(\varepsilon_0 + \bar{\varepsilon}_e^p\right)^n + (1-\alpha)\left\{B + C\left[1 - \exp\left(-D\bar{\varepsilon}_e^p\right)\right]\right\}, \tag{23}$$

where α is the corrected coefficient, A, ε_0, n denote material parameter of the Swift model, B, C, D are material parameters of the Voce model. The hardening parameters are identified from the tensile tests and are given in Table 2.

Table 2. Hardening model parameters [15]

Parameter	α	A (MPa)	ε_0	n	B (MPa)	C (MPa)	D
Value	0.58	1570	2.56×10^{-5}	0.129	548	531	92.8

The damage model parameters are calibrated by comparison between numerical simulations and experimental data of uniaxial tensile specimens [16]. The values of the parameters are shown in Table 3.

Table 3. Ductile damage model parameters

Parameter	f_0	β	θ	D_{crit}
Value	1.5×10^{-4}	2	0	50

Six Nakajima-type deep-drawn specimens are employed for numerical simulation; their dimensions and geometries are given in Fig. 2.

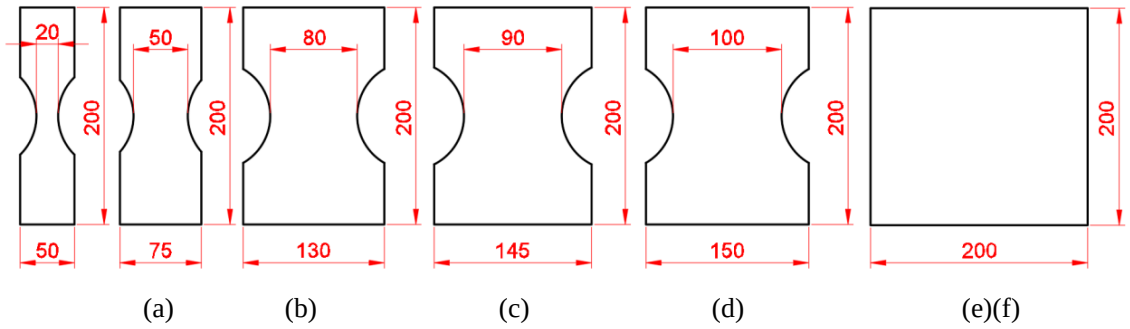

Fig. 2. Deep drawn specimens: (a) W20, (b) W50, (c) W80, (d) W90, (e) W100, (f) W200

The finite element model includes a die, holder, blank, and punch where the die, holder, and punch are assumed rigid bodies. In contrast, the blank is depicted in the deformation of realistic material. For the blank, a finite element mesh is constructed with different configurations depending on specimen geometries, as illustrated in Fig. 3 for the W100 and W50 specimens. The Coulomb friction law with a coefficient of friction of 0.05 defines the contact surface between the punch and the blank. Meanwhile, a coefficient of friction of 0.11 is adopted to define the other contact surfaces. The die is fixed whereas

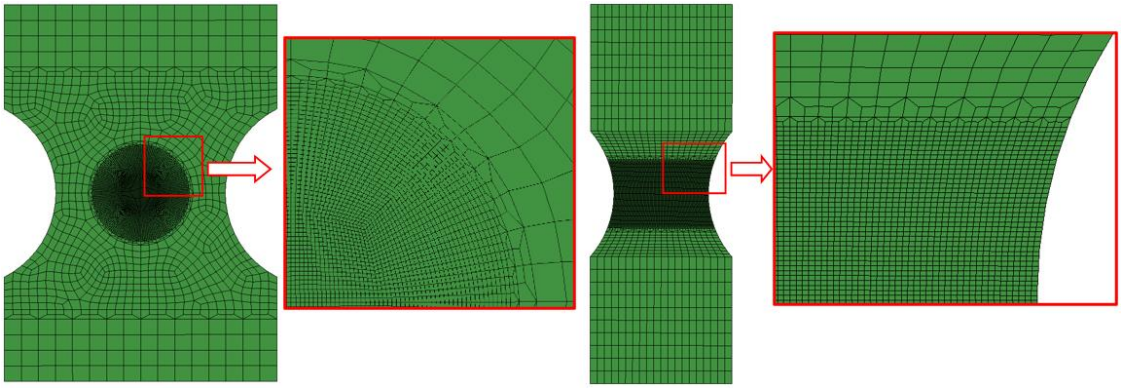

(a) (b)

Fig. 3. Illustration of finite element mesh: (a) W100 and (b) W50 specimens

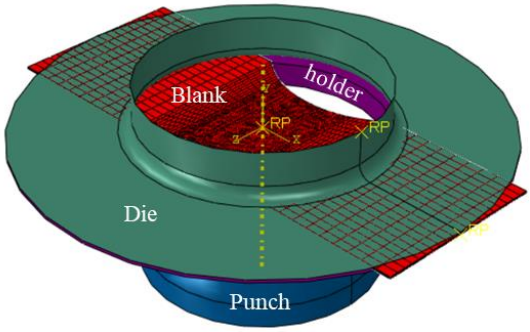

Fig. 4. Setup diagram of the Nakajima deep drawing process

a holding force of 250 kN keeps the blank. The punch is constrained by boundary conditions such that it can only move in the vertical direction until fractured initiation. The finite element model of the deep drawing process is shown in Fig. 4.

The principal strain values at the moment of local necking, which are extracted to construct a forming limit diagram (FLD) are presented in Fig. 5. The strain field of each specimen is concentrated into a narrow band at the punch top except for the W200 specimen subjected to biaxial stretch loading as shown in Fig. 5. Three strain paths are extracted at the necking region in each specimen. Their average value is used to construct a fitting window according to the ISO 12004-2-2008 standard as illustrated in Fig. 6. Based on the data fitting method, the major and minor limit strains are picked to construct the forming limit curve of DP980 steel as shown in Fig. 7. As shown in Fig. 7, the limit strain values obtained by numerical simulation using the proposed ductile damage model are in good agreement with experimental data from the literature [15].

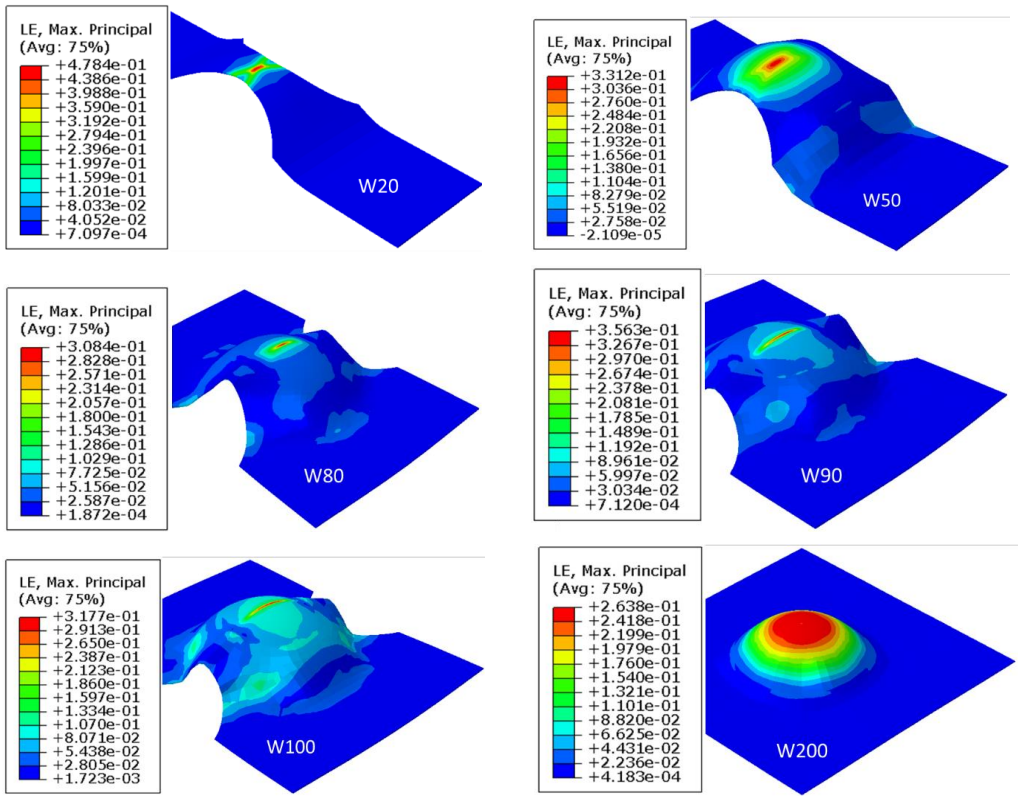

Fig. 5. The principal distributed field at the necking moment of the specimens

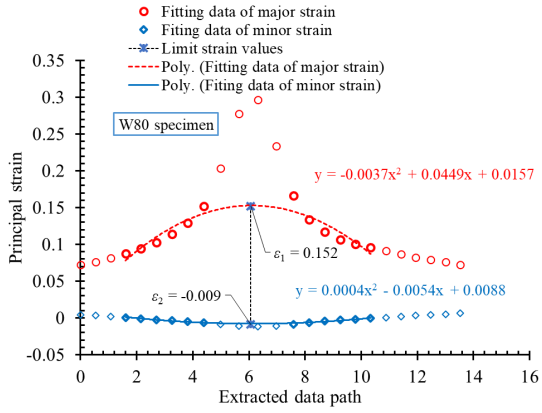

Fig. 6. Illustration of identifying limit strain values following the ISO 12004-2-2008 standard

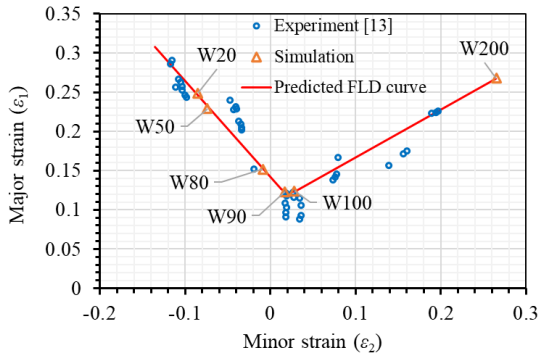

Fig. 7. Forming limit diagram of DP980 steel

4. CONCLUSION

In this paper, an enhanced ductile damage model is successfully applied to predict the forming limit of anisotropic sheet metal. Specifically, AHSS steel DP980, which is being commonly used in the civil engineering industry is adopted to validate the applicability of the novel model. The procedure for determining plastic strain limits is conducted following the ISO 12004-2-2008 standard. Accordingly, six Nakajima-type specimens are designed to describe various strain states from uniaxial tension, through plane strain, and biaxial stretch. In general, the predicted results obtained from numerical simulations are consistent with experimental data referred from the published paper. Differences between predicted results and experimental data may be due to unexpected and difficult-to-completely control factors, such as finite element mesh size, punch velocity, and friction coefficient at contact surfaces, etc. Based on the method used in this paper, the current ductile fracture model can be combined with advanced non-quadratic yield functions such as yld96 and yld2000 functions to improve the crack prediction accuracy of sheet metals with complex plastic flow anisotropy.

DECLARATION OF COMPETING INTEREST

The authors declare that they have no known competing financial interests or personal relationships that could have appeared to influence the work reported in this paper.

ACKNOWLEDGMENT

We acknowledge the University of Transport and Communications (UTC) for supporting this study.

REFERENCES

[1] F. M. Al-Abbasi and J. A. Nemes. Micromechanical modeling of dual phase steels. *International Journal of Mechanical Sciences*, **45**, (2003), pp. 1449–1465. https://doi.org/10.1016/j.ijmecsci.2003.10.007.

[2] A. L. Gurson. Continuum theory of ductile rupture by void nucleation and growth: Part I—yield criteria and flow rules for porous ductile media. *Journal of Engineering Materials and Technology*, **99**, (1977), pp. 2–15. https://doi.org/10.1115/1.3443401.

[3] L. Xue. *Ductile fracture modeling: theory, experimental investigation and numerical verification*. PhD thesis, Massachusetts Institute of Technology, (2007).

[4] L. Xue and T. Wierzbicki. Ductile fracture initiation and propagation modeling using damage plasticity theory. *Engineering Fracture Mechanics*, **75**, (2008), pp. 3276–3293. https://doi.org/10.1016/j.engfracmech.2007.08.012.

[5] N. Pathak, J. Adrien, C. Butcher, E. Maire, and M. Worswick. Experimental stress state-dependent void nucleation behavior for advanced high strength steels. *International Journal of Mechanical Sciences*, **179**, (2020). https://doi.org/10.1016/j.ijmecsci.2020.105661.

[6] Z. Li, F. Shen, Y. Liu, C. Hartmann, R. Norz, S. Müntermann, W. Volk, J. Min, and J. Lian. Anisotropic fracture behavior of the 3rd generation advanced high-strength – Quenching and Partitioning steels: Experiments and simulation. *Journal of Materials Research and Technology*, **30**, (2024), pp. 9395–9414. https://doi.org/10.2139/ssrn.4760467.

[7] N. Park, H. Huh, S. J. Lim, Y. Lou, Y. S. Kang, and M. H. Seo. Fracture-based forming limit criteria for anisotropic materials in sheet metal forming. *International Journal of Plasticity*, **96**, (2017), pp. 1–35. https://doi.org/10.1016/j.ijplas.2016.04.014.

[8] C. Nikhare, P. D. Hodgson, and M. Weiss. Necking and fracture of advanced high strength steels. *Materials Science and Engineering: A*, **528**, (2011), pp. 3010–3013. https://doi.org/10.1016/j.msea.2010.12.098.

[9] S. Zhang, W. Ding, K. Li, and S. Song. Prediction of ductile fracture for DP590 high-strength steel with a new semi-coupled ductile fracture criterion. *Journal of the Brazilian Society of Mechanical Sciences and Engineering*, **44**, (2021). https://doi.org/10.1007/s40430-021-03275-z.

[10] I. U. Aydiner, B. Tatli, and T. Yalçinkaya. Investigation of failure mechanisms in dual-phase steels through cohesive zone modeling and crystal plasticity frameworks. *International Journal of Plasticity*, **174**, (2024). https://doi.org/10.1016/j.ijplas.2024.103898.

[11] F. A. McClintock, S. M. Kaplan, and C. A. Berg. Ductile fracture by hole growth in shear bands. *International Journal of Fracture*, **2**, (1966), pp. 614–627. https://doi.org/10.1007/bf00184558.

[12] N. L. Dung. Three-dimensional void growth in plastic materials. *Mechanics Research Communications*, **19**, (1992), pp. 227–235. https://doi.org/10.1016/0093-6413(92)90070-q.

[13] L. Xue. Constitutive modeling of void shearing effect in ductile fracture of porous materials. *Engineering Fracture Mechanics*, **75**, (2008), pp. 3343–3366. https://doi.org/10.1016/j.engfracmech.2007.07.022.

[14] M. Ortiz and J. C. Simo. An analysis of a new class of integration algorithms for elastoplastic constitutive relations. *International Journal for Numerical Methods in Engineering*, **23**, (1986), pp. 353–366. https://doi.org/10.1002/nme.1620230303.

[15] K. Pack, T. Tancogne-Dejean, M. B. Gorji, and D. Mohr. Hosford-Coulomb ductile failure model for shell elements: Experimental identification and validation for DP980 steel and aluminum 6016-T4. *International Journal of Solids and Structures*, **151**, (2018), pp. 214–232. https://doi.org/10.1016/j.ijsolstr.2018.08.006.

[16] H. H. Nguyen. Ductile damage prediction of advanced high-strength sheet steel using an enhanced crack criterion. In *Proceedings of the International Conference on Sustainable Energy Technologies*, Springer Nature Singapore, (2024), pp. 405–413. https://doi.org/10.1007/978-981-97-1868-9_41.